RSC Applied Interfaces

PAPER

View Article Online
View Journal

Cite this: DOI: 10.1039/d5lf00064e

Controlling N speciation in solution synthesis of N-doped carbon materials†

Mi Yeon Byun, Lili Liu, Daniel Mejía-Rodríguez, Eric D. Walter, Zihua Zhu, Niri Govind, Tom Autrey and Maria L. Sushko *

Received 4th March 2025,
Accepted 8th June 2025

DOI: 10.1039/d5lf00064e

rsc.li/RSCApplInter

Carbon-based materials, such as graphite and its functionalized/doped derivatives, are promising lightweight layered materials for hydrogen activation and storage. Their propensity to control the thermodynamics of hydrogen binding and the kinetics of hydrogen mobility strongly depends on the speciation and the arrangement of dopants. In this study, we demonstrate precise control over dopant speciation and clustering in nitrogen-containing layered carbon materials during hydrothermal synthesis. Through extensive spectroscopic characterization and first principles simulations, we demonstrate that the formation of N-motifs can be controlled by the choice of precursor and synthesis temperature. The distinct three-dimensional architecture and porosity in graphene oxide and carbon nitride-derived materials furnish a synthetic pathway for precise control over the local and global structure of nitrogen-doped carbon materials and their activity toward the activation of molecular hydrogen.

1. Introduction

Heteroatom-doped carbon emerged as a viable low-cost alternative to Pt catalysts for hydrogen evolution reaction (HER). The studies of various dopants demonstrated that nitrogen doping dramatically improves the activity of carbon materials towards HER and that further improvements can be achieved by using co-dopants, such as boron and phosphor, to activate adjacent carbon atoms.[1–13] In addition to the electrocatalytic HER, nitrogen-modified graphitic carbons forming motifs with 3 N atom substituting next nearest neighbor carbons are thermocatalytically productive for the activation of molecular hydrogen to reduce unsaturated organics and the activation of carbon–hydrogen bonds in liquid organic hydrogen carriers (LOHCs).[14,15] For example, recent studies revealed that N-doped carbon materials (NCs) are efficient catalysts for the dehydrogenation of multiple N-heterocycles at room temperature.[15] Kinetic and computational studies suggest that C–H bonds are weaker at 3 N sites, which leads to accelerated recombination of adsorbed hydrogens into H_2. Furthermore, these active sites were predicted to lower energy barriers in every elemental step of LOHC dehydrogenation when compared to carbon materials with a random distribution of N-dopants. These findings open the opportunities for developing NCs for catalyzing dehydrogenation, enabling hydrogen storage and transfer to and from layered materials and LOHCs. However, due to the strong dependence of activity on N-motifs, it is critical to understand how to control the distribution of N during synthesis either through precursor or defect engineering to enhance the likelihood of the formation of desired N-motifs.

These findings, in both electrocatalytic HER and thermocatalytic hydrogen activation, spurred intense research into the development of synthesis methods for this class of materials. Hydrothermal synthesis of free-standing NCs uses various precursors and temperature ranges to produce NCs with a relatively low N-content of about 5%.[16–23] These free-standing N-doped carbon materials have mainly graphitic and pyridinic N with the relative ratio of these species varying depending on the details of the synthesis. Despite a significant number of reports of CN synthesis the mechanism for controlling N-speciation remains unknown hindering the development of these materials for practical applications. Furthermore, many open questions remain in understanding the mechanism of hydrogen transfer and activation on N-doped carbons and its dependence on dopant speciation and arrangement within graphitic layers.

Here we aim to fill these knowledge gaps through the detailed study of the dependence of N-speciation in free-standing layered NC-materials and the role of N-speciation in thermodynamics of hydrogen activation and transfer. Through systematic variation of synthesis conditions and detailed characterization, we demonstrate that N speciation can be controlled by designing synthesis to facilitate or

Pacific Northwest National Laboratory, Richland, WA, USA.
E-mail: maria.sushko@pnnl.gov

† Electronic supplementary information (ESI) available. See DOI: https://doi.org/10.1039/d5lf00064e

inhibit N-doping of a defect in the graphitic lattice. Through computational studies, we predict the most energetically favorable N-motifs and compare with the evolution of 3 N motifs and of our prepared free standing NC materials. Finally, we investigate the thermocatalytic activity for molecular hydrogen activation through an evaluation of hydrogen–deuterium exchange in mixtures of H_2 and D_2 gas at moderate temperatures, leading to the reversible chemisorption of molecular hydrogen.

2. Methods

Synthesis

N-GO. All chemicals used in our experiment are analytical grade and used as received without further purification. The synthesis of N-doped graphene starts from graphene oxide (GO), which was synthesized from natural graphite flake powder through a traditional Hummer's method.[24] The as-prepared GO (30 mg) was dispersed in 10 mL water with 1% $NH_3{\cdot}H_2O$, stirring continuously at 80 degrees for 10 min, and then urea (180 mg) was added to the brown colloidal solution. After stirring for 2 hours at 80 °C, the hydrogel was obtained using 7% HNO_3 and collected after centrifugation with deionized water twice and then freeze-dried for 24 h. The dried sample was pyrolyzed at 350, 550, and 800 °C for 3 h under an N_2 atmosphere.

NC. The NC was prepared using g-C_3N_4 as a template.[25] For the synthesis of g-C_3N_4, the mixture of 15 g of urea and 1 g of D.I. water were placed in a crucible with a lid and then wrapped with aluminum foil, subsequently calcining at 550 °C for 3 h with a heating rate of 3 °C min^{-1} in air.

The prepared 0.5 g of g-C_3N_4 was dispersed in 40 mL of 0.3 M D-glucose solution and stirred at 25 °C for 4 h. The suspension was transferred to a hydrothermal reactor, and heated at 180 °C for 10 h with a heating rate of 5 °C min^{-1}. After cooling down to room temperature, the suspension was filtered and washed with D.I. water and ethanol. The produced D-glucose and g-C_3N_4 composite was dried at 85 °C for 12 h in the oven. Finally, NC was obtained by pyrolysis of the D-glucose and g-C_3N_4 composite at 700 and 900 °C for 1 h with a heating rate of 5 °C min^{-1} in N_2 flow and denoted as NC*X* (*X* is calcination temperature).

Characterization

Powder XRD. Powder XRD of all as-prepared samples was performed on a Philips X'PERT Multi-Purpose Diffractometer (MPD) (PANAlytical) equipped with Cu K_α radiation operating at 50 kV and 40 mA within the 2θ range from 5° to 100°.

X-ray photoelectron spectroscopy (XPS). X-ray photoelectron spectroscopy (XPS) was used to characterize the chemical properties of CN. XPS was performed using an Al Kα X-ray source, employing a Thermo Fisher NEXSA instrument. The C 1s peak at 284.8 eV was used for calibration.

ToF-SIMS. ToF-SIMS spectra were acquired using a ToF-SIMS 5 spectrometer equipped with a 25 keV bismuth liquid metal ion gun from ION-TOF GmbH (Münster, Germany). The analysis was carried out with a Bi^{3+} beam as the primary ion under a vacuum in the range of 10^{-9} mbar during all measurements.

Raman spectroscopy. Raman spectra were recorded by using a Horiba LabRam HR spectrometer attached with an inverted optical microscope (Nikon Ti-E) (40× objective) and a HeNe laser light source (632.8 nm). All spectra were recorded in the range 150–4000 cm^{-1} using three 60 s exposure times.

Transmission electron microscopy (TEM). Transmission electron microscopy (TEM) characterization was performed using the FEI Titan 80–300 keV environmental TEM microscope. Approximately 10 μL of each TEM sample suspension was deposited onto holey carbon-coated copper grids (Lacey Carbon, 300 mesh; Ted Pella, Inc.). After allowing the carbon grids to air dry, they were mounted on a double-tilt TEM holder for the morphology observation. The chemical composition of each sample was analyzed using STEM energy-dispersive X-ray spectroscopy (EDS) with a Bruker EDS detector.

Nitrogen physisorption. N_2 adsorption and desorption isotherm analysis was performed on Micromeritics ASAP 2020. A 100 mg sample was loaded into the sample tube and subsequently degassed at 150 °C for 6 h prior to the adsorption measurements.

ICP. The metal impurity content was measured using inductively coupled plasma optical emission spectrometry (ICP-OES) with a PerkinElmer 7300DV.

***In situ* high-pressure nuclear magnetic resonance (NMR).** *In situ* monitoring of H/D exchange with NMR spectroscopy was performed under magic angle spinning conditions using WHiMS high-pressure NMR rotors developed at Pacific Northwest National Laboratory. These rotors are closed with one-way flow valves that allow gas to enter the rotor in the gas charging apparatus and remain pressurized during the NMR data collection. Rotors were charged with a mix of H_2 and D_2 gas, then immediately loaded into the NMR probe, and the temperature was adjusted to that desired for the experiment. The gas mix was created in our apparatus by filling at the desired ratio using separate sources of H_2 and D_2, then the pressure was increased to the desired experimental pressure with an Isco syringe pump. Spectra were acquired using a Varian DDR2 spectrometer console and a home-built DR 5 mm probe in an 11.7 T magnet. 1H spectra are referenced to TMS *via* the high-frequency resonance in a solid sample of adamantane (34.84 ppm), while D_2O was used as the reference and calibration for 2H experiments. Typical 2H spectra are the average of 256 transients obtained with a π/2 pulse width of 4.25 μs, pulse delay of 5 s, spectral width of 100 kHz, acquisition time of 150 ms, and spin rate of 4 kHz. All NMR spectra were processed in MestReNova, commercial software available from MestReLabs. Typical NMR spectra shown in this paper received 5 Hz of exponential apodization, a left shift of two data points, and a zero fill to 16k or 32k points before the FT.

Density functional theory (DFT) simulations. Density functional theory (DFT) simulations of the structure of CN materials were performed using periodic plane wave DFT implemented in VASP code.[26,27] Generalized gradient approximation and projected augmented wave (PAW) potentials[28] were used with PBE exchange–correlation functional[29] and the D2 Grimme dispersion correction.[30] Spin polarization was included in all calculations: 6 × 6 × 1 Gamma-centered Monkhorst–Pack grid was used for *k*-point sampling of the Brillouin zone. A plane wave cutoff of 400 eV was used.

CN materials were modeled as a 3-layer graphite slab with defects and *N*-substitutions in the top layer using 3D periodic model. A 15 Å vacuum gap between images of the basal planes was used to avoid interactions between periodic images. Common defects, such as C vacancy (CV), 5–8–5, and Stone–Wales defects, were introduced in the basal plane. A series of *N*-substitutions were considered to compare the energetic preference of *N* substitution. All atoms were fully relaxed during structural optimization. The convergence criterion for geometric relaxation was set to 0.01 eV $Å^{-1}$.

Core-level XPS simulations. Core-level XPS simulations of various CN clusters were performed using the Gaussian-basis GW implementation[31] in the NWChem code.[32] The geometries of the clusters were first optimized using the r^2-SCAN exchange–correlation functional[33] with Grimme's D3 empirical dispersion corrections[30,34] with Becke–Johnson damping enabled. Core-level N 1s and C 1s binding energies were subsequently obtained at the one-shot G_0W_0 level using hybrid PBEh,[35,36] with a 45% admixture of exact exchange, mean-field solutions as starting points. To diminish the likelihood of (quasi)linear dependencies, all simulations used a basis set developed to describe crystalline solids, graphene-dcm-TZVP,[37] for C atoms combined with the standard def2-TZVP triple-zeta basis set for N and H.[38]

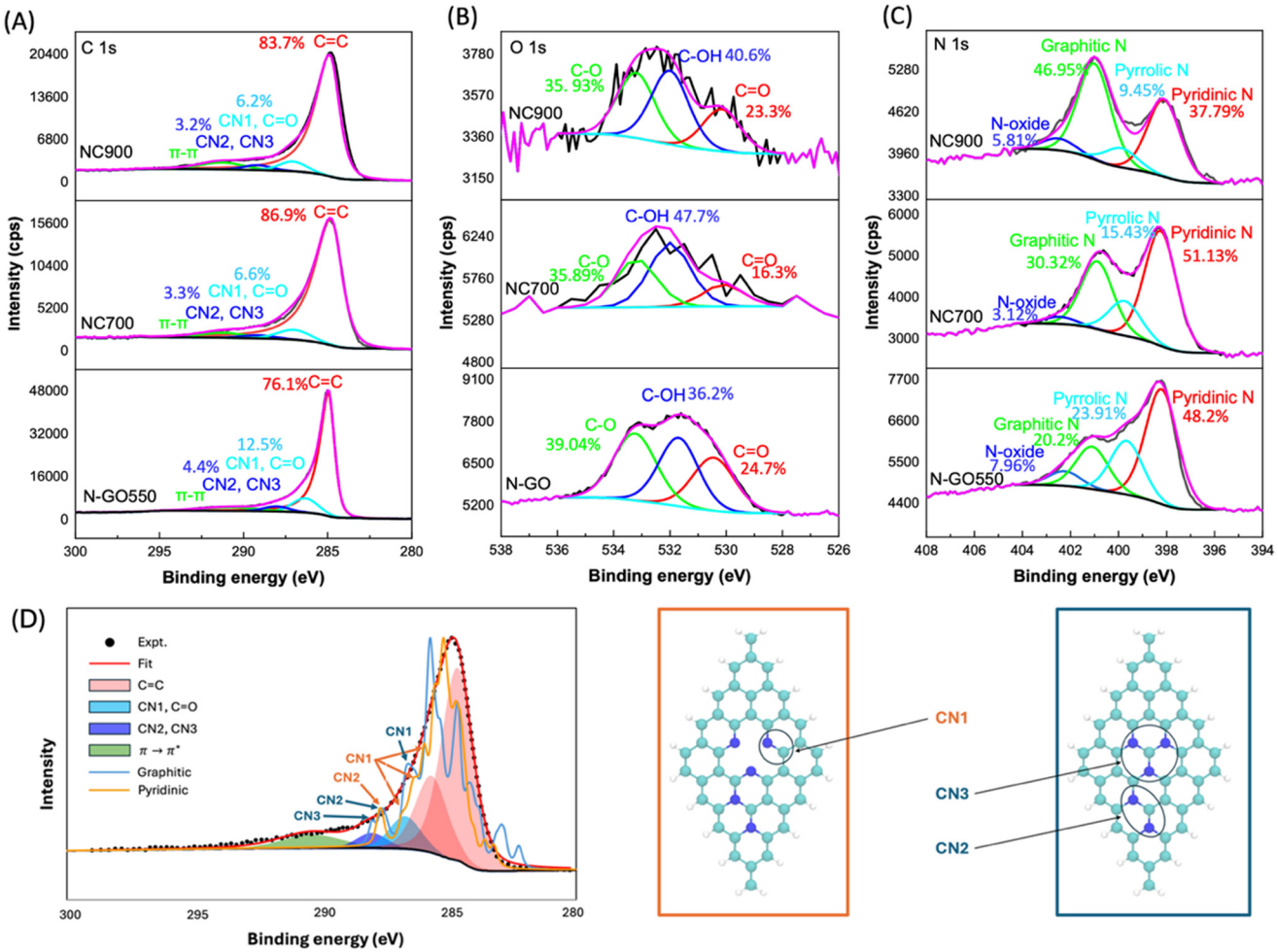

Fig. 1 Speciation in CN materials derived from their XPS spectra of (A) C 1s, (B) O 1s, and (C) N 1s. (D) Simulated XPS C 1s spectrum and the fitting of C 1s spectrum of NC700 based on theoretical peak assignment. Peaks at 284.7, 286.2, 288.4, and 290.7 eV in C 1s spectra correspond to C=C, CN1/C=O, CN2/CN3, and π–π^* species, respectively. The O 1s peaks at 530.2, 532.1, and 533.4 eV, corresponding to C=O, C–OH, and C–O, respectively. The N 1s peaks at 398.5, 399.9, 401.1, and 402.4 eV are assigned to pyridinic N, pyrrolic N, graphitic N, and N-oxide, respectively. Carbon atoms are shown as cyan spheres and N atoms as blue spheres in the structures of clusters with pyridinic (orange border) and graphitic (blue border) Ns in (D).

3. Results and discussion

N-speciation in CN materials

CN materials were synthesized using two approaches described in detail in the Methods section: conceptually, the first method uses graphene oxide flakes as a precursor for graphitic material and urea for *N*-functionalization. The second method uses graphitic carbon nitride precursor to synthesize free-standing layered material. Both methods produce layered graphitic materials with approximately 7–14 at% N content. The main difference, however, is in the type of N-doping in these materials (Fig. 1). In graphene oxide-derived NC (N-GO) most N is pyridinic or pyrrolic and about 20% is graphitic. That is, most N functionalization of graphene oxide occurs at vacancy sites as evidenced by the change in composition of the precursor material during synthesis (Table 1). The composition of GO changes from 75.2% C, 24.7% O, and 0.1% N to 87.7% C, 4% O, and 8.1% N during its transformation into N-GO550. Urea serves as both a nitrogen source and a chemical reductant during the synthesis. The decrease in oxygen content from 24.7% in GO to 4% in N-GO suggests that a substantial portion of the oxygen-containing groups in GO, such as hydroxyl, epoxide, and carboxyl groups, are reduced or react with the NH_2 group of urea to form C–N bonds, resulting in nitrogen doping during the annealing process.[39] At lower temperatures, the epoxide groups provide reactive electrophilic sites for reaction with nucleophilic nitrogen in urea and as the temperature is increased, it is likely that phenolic groups are reduced, leading to defects that react with NH_3 released from decomposition of urea to form pyridinic N-motifs. Computational analysis (*vide infra*) suggests that carbon defects are stabilized by the addition of multiple nitrogen atoms, providing a pathway for the production of segregated nitrogen in 2D carbon materials. The increase in N content to 8.1% in N-GO indicates successful doping. Nitrogen atoms react with oxygen-containing groups decorating defects and edges of graphene oxide to form pyridinic or pyrrolic nitrogen. The relative pyridinic to graphitic N only weakly depends on annealing temperature in the range of 350 to 800 °C (see Fig. S1 and S2† for details), supporting the general nature of the proposed mechanism.

In carbon nitride-derived material (NC) the percentages of pyridinic and graphitic N strongly depend on the calcination temperature due to the differences in the mechanism of N-doping within this approach. During N-GO formation, the enhanced reactivity of vacancy sites functionalized with hydroxyl and carboxyl groups promote preferential N incorporation at defects, giving rise to a higher concentration of pyridinic or pyrrolic N. In contrast, nitrogen-rich (55% N) g-C_3N_4 is used as a template for the formation of NC. When g-C_3N_4 covered with D-glucose is heated above 710 °C, it decomposes into nitrogen-containing compounds such as C_2N_2, C_3N_2, C_3N_3, CNH_2, and NH_3 during the carbonization process.[40,41] These nitrogen sources can substitute carbon atoms in the lattice, producing pyridinic N, pyrrolic N, graphitic N, and N-oxide. The ratio of pyridinic N to graphitic N can change depending on the annealing temperature.[42,43] The nitrogen content decreased from 14.8% to 7.1% as the calcination temperature increased from 700 °C to 900 °C. This trend is consistent with similar results reported in other studies, which also observed a reduction in N content with increasing temperatures, likely due to thermal stability issues at higher temperatures.[44] This temperature-induced decrease in N content is accompanied by the reduction in the pyridinic to graphitic N ratio (Fig. 1). Reflecting this change in N speciation, the C/N atomic percentage in the NC materials increased from 5.7% to 12.9% as the temperature increased from 700 °C to 900 °C. Specifically, the atomic percentage of pyridinic N decreased significantly from 7.5% to 2.6%, while the graphitic nitrogen percentage changed slightly, from 4.5% to 3.3% (Fig. S1†). The decrease in pyrrolic N content is even more pronounced, dropping from 15.4% to 9.5%. The observation is consistent with the reported thermal instability of pyrrolic N,[45] with decomposition occurring at temperatures around 700 °C. Thus, pyrrolic N is more likely to be directly removed from the carbon structure during high-temperature annealing, which furnishes a path for controlling N-speciation in CN materials.

To understand finer details of N-speciation and a possible formation of stable N-motifs, XPS spectra for various graphitic and pyridinic N arrangements in graphene flakes were simulated using the Gaussian-basis GW approach. As expected, C 1s binding energies increase with the number of bonded N atoms, regardless of the nitrogen atom type (pyridinic or graphitic). The 1s binding energy of C atoms bonded to a single graphitic N (CN1) is shifted by 2.1 eV from the main peak. For most C atoms bonded to the pyridinic N CN1, peaks appear at lower binding energies 0.3 eV. For most carbons, the pyridinic CN1 peak is shifted by 0.3 eV down from the graphitic CN1. The effect of the local environment in the outer coordination sphere of C atoms also affects the CN1 peak position. The pyridinic CN1s neighboring graphitic N form a separate peak positioned between pyridinic and graphitic CN1 peaks. All 1s energies of C atoms bonded to two (CN2) or three (CN3) N atoms appear bundled together with an average chemical shift of 3.4 eV (Fig. 1D).

Table 1 Composition of precursor and CN materials

	C (at%)	O (at%)	N (at%)
GO	75.2	24.7	0.1
N-GO350	84.0	5.6	10.4
N-GO550	87.7	4.0	8.1
N-GO800	89.9	7.1	3.0
g-C_3N_4	43.8	0.7	55.5
NC700	83.9	1.3	14.8
NC900	91.9	1.0	7.1

These findings indicate N clustering in CN materials, with about half of the nitrogens forming CN2 and CN3 motifs in NC700 and NC900. A higher content of vacancies and a higher fraction of CN1 species in N-GO550 point to the prevalence of N2 and N3 motifs at vacancy sites. This conclusion is further supported by the larger fraction of non-graphitic nitrogen (Fig. 1C).

Relative formation energies of various N-motifs on graphitic surfaces were calculated using DFT to gain insights into possible arrangements of pyridinic and graphitic N-dopants in these materials. Previous studies reported the comparative analysis of the formation energy of N-motifs on stoichiometric graphene. They identified that the most energetically favorable arrangements of graphitic N are N substituting three nearest neighbors of the surface C.[15] By design, this study did not encompass the motifs with pyridinic N considered here. We studied representative N arrangements at common defect sites: single vacancy (SV), 5–8–5, and Stone–Wales (SW) defects. Relative formation energies for Nx motifs, with x = 1, 2, 3, 4, were calculated using x graphitic N separated by at least 8 Å as reference states. Simulations predict that pyridinic N is favored at single vacancy sites and the relative formation energy for pyridinic N decreases with the increase in the number of N at the site (Fig. 2). For example, substituting 1, 2, and 3 carbons with N at the vacancy results in 0.14, 1.2, and 2.21 eV energy gain per N compared to random substitution at graphitic sites. The resulting N-motif is similar to the lowest energy motif of graphitic N (Fig. 2A). However, undercoordinated pyridinic N at the vacancy site is expected to be more reactive towards hydrogen activation and transfer. The most energetically favorable N-motif at 5–8–5 vacancy contains four pyridinic N, and the relative energy gain per N is even bigger than that for SV (Fig. 2A). *N* substitution at the SW defect, which produces pyrrolic N, is less energetically favorable than at other defects (Fig. 2A). In the absence of other defects at graphite terraces that contain sites for forming pyrrolic N, the most likely occurrences of such N are at the edges of graphitic sheets. The result correlates well with negligible content of pyrrolic N in either N-GO or NC.

Simulations also revealed that 5–8–5 defects stabilize the CN_3 motifs with the energetic preference compared to the same motif at a defect-free terrace of 1.035 eV (Fig. 2B). Coupled with the 0.08 eV preference for *N*-substitution at 5–8–5 vacancy sites, the possible pathway for the sequential substitution of C with N may involve the initial substitution of C with N at the hexagons of the 5–8–5 defect, followed by the substitution of the next nearest neighbor carbons. These differences in the relative energies predict that the probability of migrating pyridinic N dopants to graphitic sites is negligible and, therefore, unlikely in the synthesis temperature range of 350–800 °C. Specifically, the minimum energy difference between these species was determined to be 0.14 eV, corresponding to the thermal energy at 1350 °C. However, annealing the CN materials at temperatures above 900 °C results in a significant loss of N (Table 1), suggesting that control over N speciation must be driven by the choice of precursor and not post-synthesis annealing.

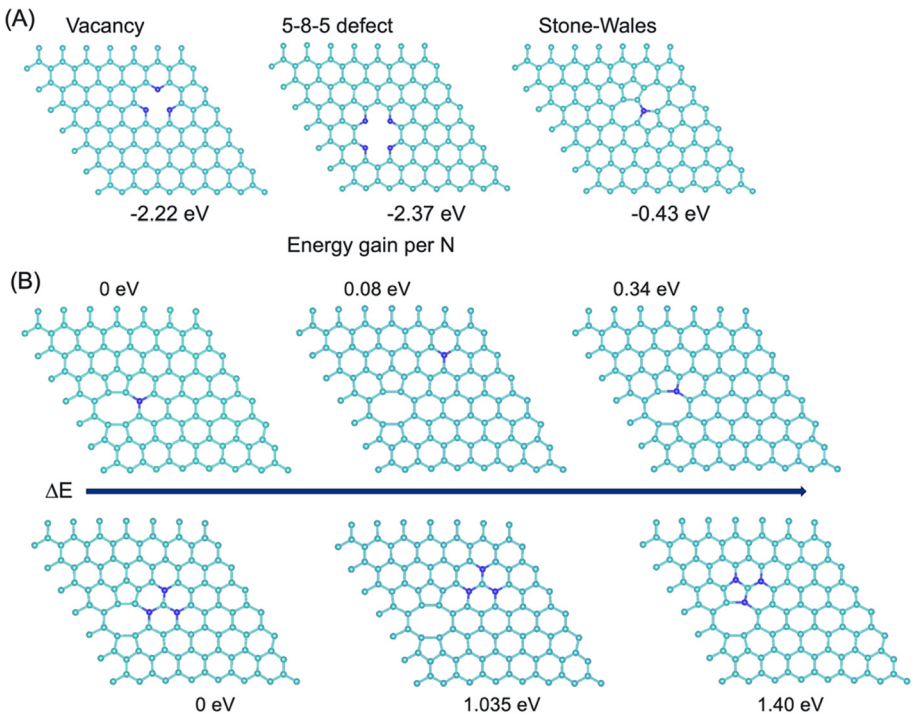

Fig. 2 Most stable N-motifs at defect sites. (A) Lowest energy configurations for N-motifs at single vacancy, 5–8–5, and Stone–Wales defects. (B) Relative energetics of a single N-substitution and the formation of CN_3 motif at 5–8–5 defect. Carbon atoms are shown as cyan spheres and N atoms as blue spheres.

ToF-SIMS experiments support the conclusion of N clustering in N-GO and, to a lesser extent, NC (Fig. 3). The SIMS analysis identified the prevalence of graphitic N in both samples (red symbols in Fig. 3A). However, the N-GO has a significant fraction of C_2N_3 and CN_2 clusters, with the C_2N_3 content only ~10 times smaller than that of graphitic N. Given that the total N-content is only about 8.1 at% and about 60% of Ns are pyridinic, SIMS results point to the prevalence of N clustering at defect sites in N-GO. In contrast, a clear prevalence of graphitic N is found in NC material, with most species identified as C_3N (Fig. 3).

Structure and porosity of N-GO and NC

Detailed characterization of the N-GO and NC materials demonstrated overall similar structure and porosity. The main difference between these materials is the N-speciation discussed in the previous section and the size of graphitic domains. The structure of the N-GO was characterized by powder XRD and TEM. The pristine GO shows sharp peaks at 2θ of 13° and 43°, representing the (002) and (100) reflection of GO structure, which shows the interlayer spacing in pristine GO is around 7.9 Å (Fig. 4). After the reduction of GO in the presence of urea in the N_2 atmosphere at 550 °C, the (002) peak redshifted, indicating a gradual decrease in the interlayer spacing. The decrease in the interlayer spacing is more pronounced in samples synthesized at higher temperatures, likely due to the more efficient removal of oxygen-containing functional groups from GO.

The g-C_3N_4 shows two peaks at 13.1° and 27.6°, corresponding to the (100) and (002) plane, which are attributed to interlayer stacking of aromatic rings and triazine units.[46] The NC700 and NC900 show two peaks at 24° and 44° corresponding to the (002) and (100) phase of graphite structure with the absence of g-C_3N_4 indicating its complete decomposition at temperatures above 700 °C.

The defect structure in CN materials was further characterized using Raman spectroscopy (Fig. 4C). The as-prepared GO and N-GO exhibited two distinct peaks. The typical D band located at around 1350 cm^{-1} represents the edges, defects, and disordered carbon sites, and the G band centered at 1590 cm^{-1} is assigned to the in-plane stretching of C–C bond between sp^2-C atoms. Therefore, the ratio of the D band and G band (I_D/I_G) intensity for GO materials indicates the fraction of disordered carbon and defect level. The intensity ratio (I_D/I_G) of N-GO materials is higher than that of GO, indicating N incorporation into the graphitic lattice. *N* substitution of carbon atoms in the graphitic lattice can disrupt the regular hexagonal arrangement of carbon atoms, leading to local distortions and defects in the lattice. On the other hand, N atoms may also occupy interstitial sites within the carbon lattice, which can create additional strain and disturb the regular structure of the carbon materials. In contrast, NC700 and NC900 exhibit a higher intensity of the G band than the D band, signifying a more graphitic structure.[25,47] Further analysis using EDS mapping of the elemental distribution of C, N, and O in CN materials reveals no clear segregation of species (Fig. 5). This does not preclude the formation of N-motifs but rules out predominant N decoration of domain edges and supports XPS finding of N incorporation into graphitic structures. TEM micrographs also reveal significant differences in the mesoscale pore structure of materials derived using different precursors (Fig. 5). N-GO550 has elongated pores between large-area two-dimensional multilayers, while NCs have a more compact structure with smaller domains. These differences in the mesoscale structure can be attributed to the impact of the structure of carbon precursor on CN architecture. N-GO550 was derived from the GO precursor with large-area two-dimensional domains. N doping largely preserved this initial mesoscale structure by mainly reacting with functional groups of GO. Conversely, NC700 and NC900 were synthesized using g-C_3N_4 as a precursor and nitrogen-rich structural template. The D-glucose-coated g-C_3N_4 was dehydrated into 5-hydroxymethylfurfural and then condensed into hydrochar during hydrothermal synthesis.[48] As the temperature increased, the g-C_3N_4 in the hydrochar

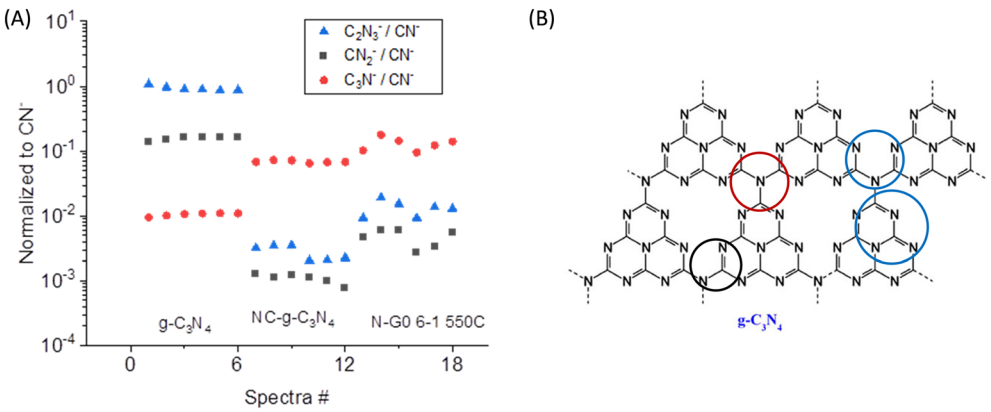

Fig. 3 N-clustering in CN materials as revealed by SIMS characterization. (A) SIMS data for the reference g-C_3N_4, NC900, and N-GO550. (B) Possible structural motifs.

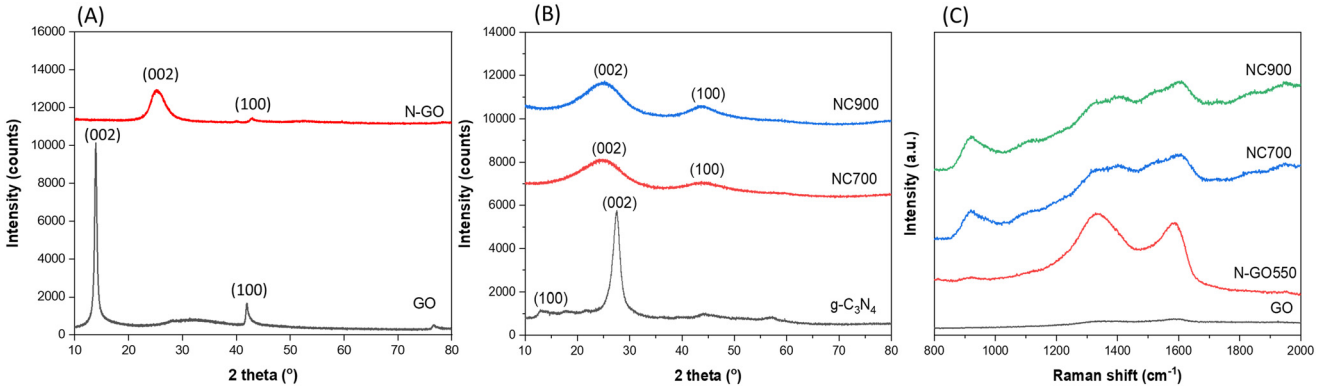

Fig. 4 Crystal structure and defects in CN materials. XRD patterns of (A) pristine GO and N-GO550 and (B) g-C_3N_4, NC700, and NC900. (C) Raman spectra of GO and CN materials.

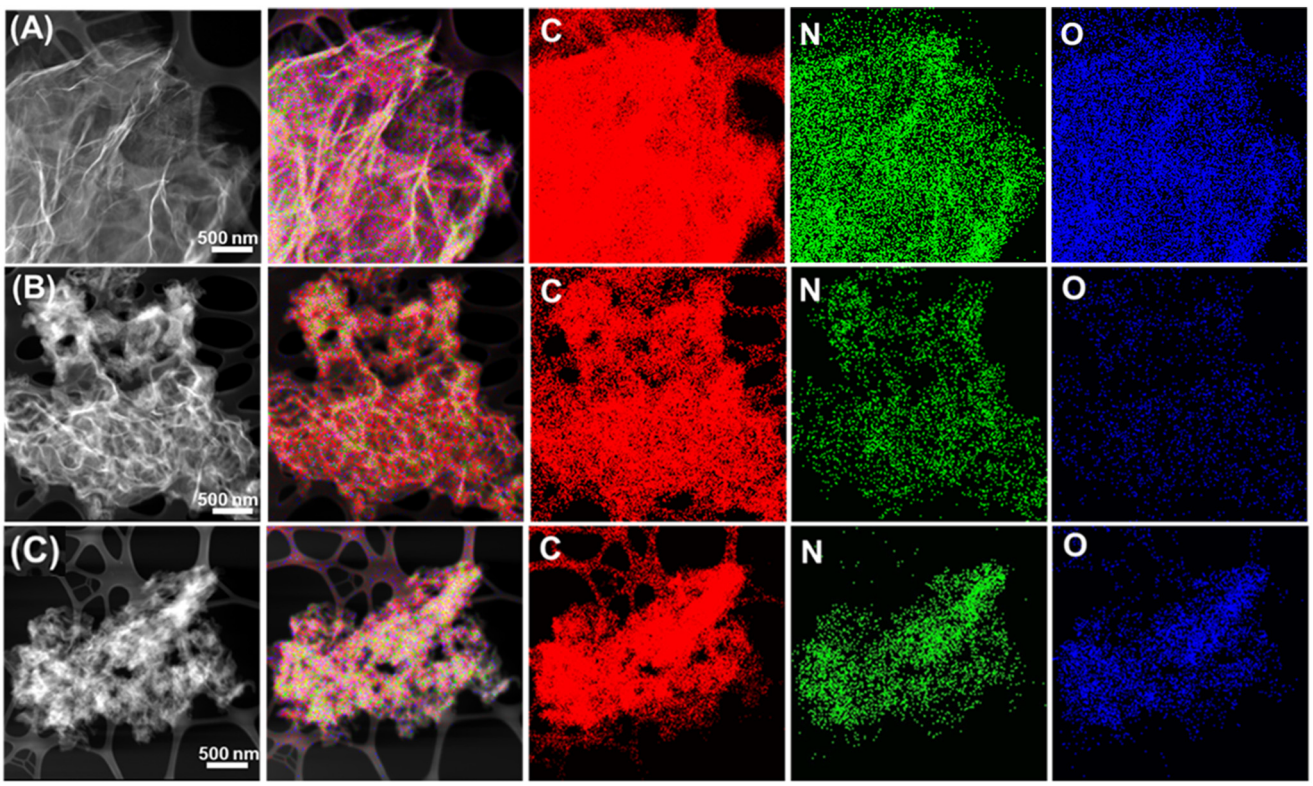

Fig. 5 Elemental distribution in CN materials. EDS mapping of (A) N-GO550, (B) NC700, (C) and NC900.

gradually decomposed and formed nitrogen-doping sites within the carbon lattice with smaller graphitic domains, as evidenced by TEM characterization (Fig. 5), with the produced gases contributing to templating the mesoporous structure with higher surface area and larger pore volume. The latter effect is less pronounced in NC900 synthesized at a higher temperature, which likely promoted faster removal of gases from the voids between graphitic domains and resulted in mesoporous architecture with a smaller surface area and pore volume than in NC700.

Surface area analysis using nitrogen physisorption supports these conclusions and provides further quantification of pore distribution inaccessible with TEM (Fig. 6). The N_2 adsorption–desorption isotherms of N-GO550, NC700, and NC900 are type IV with H3 hysteresis loops, which indicate mesoporous materials and wedge-shaped pore structures (Fig. 6). The hysteresis loop extends to higher relative pressure in NC700 than in NC900, indicating the prevalence of larger mesopores. We observed that N-GO550 has a surface area and pore volume of 65.6 $m^2\ g^{-1}$ and 0.19 $cm^3\ g^{-1}$, respectively, while NC700 and NC900 exhibit higher surface areas (319.9 and 258.5 $m^2\ g^{-1}$) and larger pore volumes (0.67 and 0.50 $cm^3\ g^{-1}$) (Table 2).

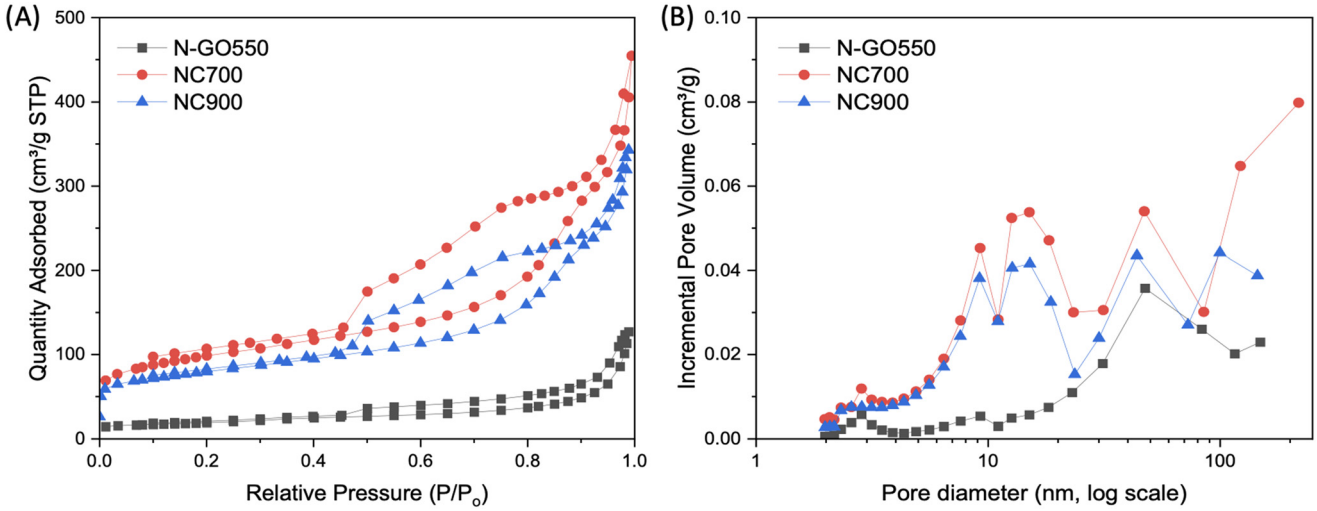

Fig. 6 Mesoscale structure of CN materials. (A) N_2 adsorption–desorption isotherm of N-GO550, NC700 and NC900. (B) Calculated porosity of N-GO550, NC700 and NC900.

Isotope exchange in CN materials

These differences in porosity and N-speciation between N-GO and NC materials affect their propensity towards hydrogen chemisorption. Previously, various carbon blacks – including nitrogen-doped carbon – have been shown to catalyze H/D exchange.[49] Because the linewidth gas phase spectrum of H_2 is of the same order or larger than the splitting of HD, previous NMR studies used linewidth analysis of the gas phase spectrum or dissolved the product gas in a solvent where the spectra are easily separable.[50] In this work, we take advantage of the fact that the gas phase spectrum narrows as the pressure increases – at 25 bar it is approximately 13 Hz, while the splitting of the HD doublet is ~40 Hz. We found the 2H spectrum to be much more useful than the 1H spectrum, as it had no background from the probe or residual protons in the sample. Additionally, the doublet of the HD product ($J \sim 40$ Hz) was much easier to deconvolute from the D_2 starting material than the corresponding HD triplet from the overlapping singlet of the H_2 in the 1H spectrum. The identity of the change in the spectrum was confirmed to be from HD by recording both 1H and 2H spectra with and without decoupling the corresponding nuclei (Fig. S3†). In initial tests, we compared the effectiveness of our materials at several temperatures, with some showing no detectable exchange at 20–80 °C over a day. Therefore, we chose to compare the relative rate of exchange at 144 °C (Fig. 7A). Approximately 5 mg (2.5 mg in the case of the much less dense N-GO) was placed in a 5 mm rotor and pressurized with a 2 : 1 mix of H_2/D_2 to 25 bar. An internal volume of 140 ml corresponds to 0.048 mmole of D_2 and 0.096 mmole of H_2 (for comparison, 5 mg of 12C would be 0.417 mmole). The 2H NMR spectrum was collected every 20 minutes over 12 hours (Fig. 7B and C). The initial rate was determined by area normalizing the spectra and then calculating a difference spectrum at the 1 hour time point, subtracted from the initial spectrum. Loss of D_2 manifested as a negative tending peak in the center, while growth in HD could be seen from a pair of flanking positive peaks in the difference spectrum (Fig. S4†). Integration showed that positive and negative areas were equal (within the limitations of S/N). The relative initial rate was calculated as the increase in the fraction of HD over the first hour, where the change in reactants was less than 5% to ensure pseudo-first order conditions.

Table 2 Structure and porosity of CN materials

	Surface area ($m^2\ g^{-1}$)	$V_{meso+macro}$ ($cm^3\ g^{-1}$)	V_{micro} ($cm^3\ g^{-1}$)	Average pore diameter (nm)
N-GO550	65.6	0.19	0.01	12.0
NC700	319.9	0.67	0.05	8.0
NC900	258.5	0.50	0.05	8.2

The results reveal that all nitrogen-doped carbons show higher reaction rates than a commercial high surface area carbon black (surface area 230 $m^2\ g^{-1}$).

Previous studies reported the enhancement of the activity of N-doped carbon materials towards hydrogen and it was expected that Vulcan carbon, which served as a N-free reference, would have the lowest exchange rate. The observed differences in H/D exchange rates in N-GO, NC700, and NC900 are likely to reflect the differences in N arrangement and speciation. XPS experimental and theoretical C 1s spectra indicate higher content of N3-motifs in N-GO550 and NC900 compared to NC700. These motifs create a local electron-rich environment promoting H/D exchange. XPS spectra of NC700, in contrast, do not show a significant presence of N3-motifs with the prevalent N-species are isolated graphitic N (C–N) and N2-motifs (Fig. 1), hence slower H/D exchange in NC700. The finer difference between N-GO550 and NC900 stems from the differences in N-speciation within N3-motifs. In N-GO materials, the largest fraction of N species is

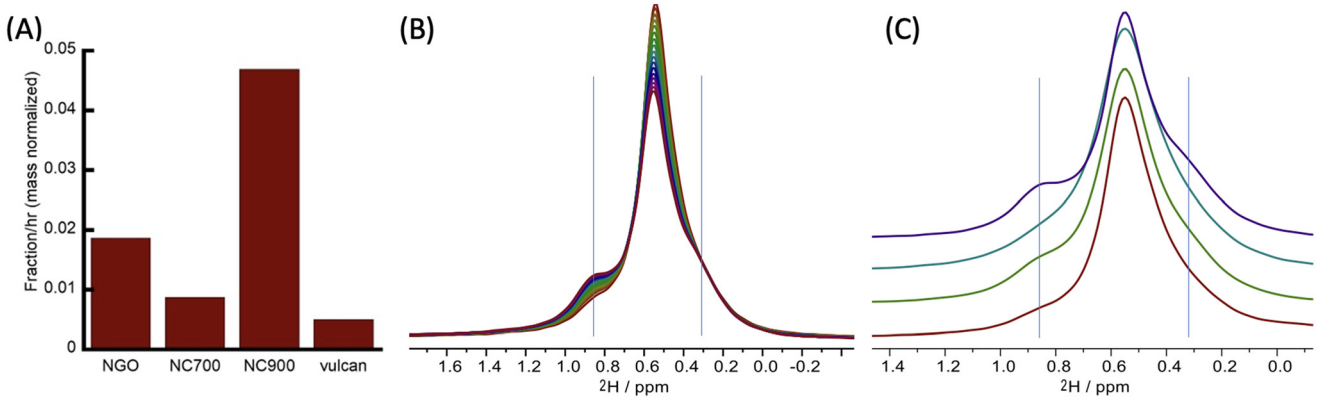

Fig. 7 H/D exchange in carbon materials detected by *in situ* NMR. (A) Initial rates of exchange at 144 °C and 375 psi total pressure, H_2/D_2 ratio 2 : 1. Normalized for carbon mass (5 mg), N-GO550 mass 2.5 mg, all others ~5 mg. (B) 2H spectra of reaction on NC900, (C) final spectrum for all reactions (17th hour), NC900 (blue), NC700 (teal), N-GO550 (green), and Vulcan carbon (red). Gray vertical lines show the position of HD product peaks.

pyridinic N, some of which form an N3-motif around C vacancy. Instead, in NC900 the N3-motifs are mainly populated by graphitic N.

4. Conclusions

The study provides insights into synthetic pathways for controlling the structure and dopant speciation and clustering in free-standing carbon materials. We showed that the choice of carbon precursor not only defines materials' architecture and porosity but also affects the speciation of N-dopants and clustering to form various N-motifs. The materials derived from graphene oxide form extended graphitic domains. *N* substitution predominantly at defect sites leads to a large fraction of pyridinic N at vacancy sites, with the most stable N3 and N4 motifs decorating single vacancy and 5–8–5 defects, respectively. The most common motif in carbon nitride-derived materials (NCs) is CN3, which is analogous to N3 configuration at a single vacancy site. The increase in annealing temperature results in a loss of isolated graphitic N, thereby increasing the relative content of CN3 motifs, enhancing NCs' activity. N3 and CN3 motifs have different local electron-rich environments, which control hydrogen activation kinetics. These complementary synthesis approaches, thereby, provide a method for controlling N speciation at constant N-content for fine-tuning the activity of N-doped carbon materials for hydrogen storage.

Data availability

The data supporting this article have been included as part of the ESI.†

Conflicts of interest

There are no conflicts to declare.

Acknowledgements

This research was performed at the Pacific Northwest National Laboratory (PNNL) with support from the U.S. Department of Energy (DOE), Office of Science, Basic Energy Sciences (BES), Division of Materials Sciences and Engineering, FWP 80110. XPS simulations were supported by the DOE BES, Division of Chemical Sciences, Geosciences and Biosciences under Center for Scalable Predictive methods for Excitations and Correlated phenomena (SPEC), which is funded as part of the Computational Chemical Sciences (CCS), FWP 70942. XRD and TEM experiments were performed under user proposal 61041 at the Environmental Molecular Sciences Laboratory (EMSL), a DOE, SC, Office of Biological and Environmental Research user facility located at PNNL. Simulations were performed using the resources of the National Energy Research Scientific Computing Center, a DOE Office of Science User Facility supported by the Office of Science of the U.S. Department of Energy under Contract No. DE-AC02-05CH11231 using NERSC award BES-ERCAP0027895. PNNL is operated by Battelle for the U.S. DOE under contract no. DE-AC05-76RLO1830.

References

1 M. D. Allendorf, Z. Hulvey, T. Gennett, A. Ahmed, T. Autrey, J. Camp, E. S. Cho, H. Furukawa, M. Haranczyk and M. Head-Gordon, An assessment of strategies for the development of solid-state adsorbents for vehicular hydrogen storage, *Energy Environ. Sci.*, 2018, **11**(10), 2784–2812, DOI: **10.1039/C8EE01085D**.

2 M. Batzill, The surface science of graphene: Metal interfaces, CVD synthesis, nanoribbons, chemical modifications, and defects, *Surf. Sci. Rep.*, 2012, **67**(3–4), 83–115, DOI: **10.1016/j.surfrep.2011.12.001**.

3 X.-K. Kong, C.-L. Chen and Q.-W. Chen, Doped graphene for metal-free catalysis, *Chem. Soc. Rev.*, 2014, **43**(8), 2841–2857, DOI: **10.1039/c3cs60401b**.

4 X. Wang, G. Sun, P. Routh, D.-H. Kim, W. Huang and P. Chen, Heteroatom-doped graphene materials: syntheses, properties and applications, *Chem. Soc. Rev.*, 2014, **43**(20), 7067–7098, DOI: **10.1039/c4cs00141a**.

5 S. T. Skowron, I. V. Lebedeva, A. M. Popov and E. Bichoutskaia, Energetics of atomic scale structure changes in graphene, *Chem. Soc. Rev.*, 2015, **44**(10), 3143–3176, DOI: **10.1039/c4cs00499j**.

6 D. S. Pyle, E. M. Gray and C. J. Webb, Hydrogen storage in carbon nanostructures via spillover, *Int. J. Hydrogen Energy*, 2016, **41**(42), 19098–19113, DOI: **10.1016/j.ijhydene.2016.08.061**.

7 Q. Fu and X. Bao, Surface chemistry and catalysis confined under two-dimensional materials, *Chem. Soc. Rev.*, 2017, **46**(7), 1842–1874, DOI: **10.1039/c6cs00424e**.

8 R. Dong, T. Zhang and X. Feng, Interface-Assisted Synthesis of 2D Materials: Trend and Challenges, *Chem. Rev.*, 2018, **118**(13), 6189–6235, DOI: **10.1021/acs.chemrev.8b00056**.

9 X. Li and L. Zhi, Graphene hybridization for energy storage applications, *Chem. Soc. Rev.*, 2018, **47**(9), 3189–3216, DOI: **10.1039/c7cs00871f**.

10 B. Qiu, M. Xing and J. Zhang, Recent advances in three-dimensional graphene based materials for catalysis applications, *Chem. Soc. Rev.*, 2018, **47**(6), 2165–2216, DOI: **10.1039/c7cs00904f**.

11 H. Xu, L. Ma and Z. Jin, Nitrogen-doped graphene: Synthesis, characterizations and energy applications, *J. Energy Chem.*, 2018, **27**(1), 146–160, DOI: **10.1016/j.jechem.2017.12.006**.

12 F. Joucken, L. Henrard and J. Lagoute, Electronic properties of chemically doped graphene, *Phys. Rev. Mater.*, 2019, **3**(11), 110301, DOI: **10.1103/PhysRevMaterials.3.110301**.

13 Y. He, S. Liu, C. Priest, Q. Shi and G. Wu, Atomically dispersed metal–nitrogen–carbon catalysts for fuel cells: advances in catalyst design, electrode performance, and durability improvement, *Chem. Soc. Rev.*, 2020, **49**(11), 3484–3524, DOI: **10.1039/c9cs00903e**.

14 Z. Luo, R. Nie, V. T. Nguyen, A. Biswas, R. K. Behera, X. Wu, T. Kobayashi, A. Sadow, B. Wang and W. Huang, *et al.*, Transition metal-like carbocatalyst, *Nat. Commun.*, 2020, **11**(1), 4091, DOI: **10.1038/s41467-020-17909-8**.

15 H. Hu, Y. Nie, Y. Tao, W. Huang, L. Qi and R. Nie, Metal-free carbocatalyst for room temperature acceptorless dehydrogenation of N-heterocycles, *Sci. Adv.*, 2022, **8**(4), eabl9478, DOI: **10.1126/sciadv.abl9478**.

16 S. Agnoli and M. Favaro, Doping graphene with boron: a review of synthesis methods, physicochemical characterization, and emerging applications, *J. Mater. Chem. A*, 2016, **4**(14), 5002–5025, DOI: **10.1039/C5TA10599D**.

17 Q. Li, M. Liu, Y. Zhang and Z. Liu, Hexagonal Boron Nitride–Graphene Heterostructures: Synthesis and Interfacial Properties, *Small*, 2016, **12**(1), 32–50, DOI: **10.1002/smll.201501766**.

18 N. Talukder, Y. Wang, B. B. Nunna and E. S. Lee, Nitrogen-doped graphene nanomaterials for electrochemical catalysis/reactions: A review on chemical structures and stability, *Carbon*, 2021, **185**, 198–214, DOI: **10.1016/j.carbon.2021.09.025**.

19 S. Beniwal, J. Hooper, D. P. Miller, P. S. Costa, G. Chen, S.-Y. Liu, P. A. Dowben, E. C. H. Sykes, E. Zurek and A. Enders, Graphene-like Boron–Carbon–Nitrogen Monolayers, *ACS Nano*, 2017, **11**(3), 2486–2493, DOI: **10.1021/acsnano.6b08136**.

20 J. Lu, K. Zhang, X. Feng Liu, H. Zhang, T. Chien Sum, A. H. Castro Neto and K. P. Loh, Order–disorder transition in a two-dimensional boron–carbon–nitride alloy, *Nat. Commun.*, 2013, **4**(1), 2681, DOI: **10.1038/ncomms3681**.

21 L. Zhao, R. He, K. T. Rim, T. Schiros, K. S. Kim, H. Zhou, C. Gutiérrez, S. P. Chockalingam, C. J. Arguello and L. Pálová, *et al.*, Visualizing Individual Nitrogen Dopants in Monolayer Graphene, *Science*, 2011, **333**(6045), 999–1003, DOI: **10.1126/science.1208759**.

22 X. Wang, G. Sun, P. Routh, D.-H. Kim, W. Huang and P. Chen, Heteroatom-doped graphene materials: syntheses, properties and applications, *Chem. Soc. Rev.*, 2014, **43**(20), 7067–7098, DOI: **10.1039/C4CS00141A**.

23 X.-K. Kong, C.-L. Chen and Q.-W. Chen, Doped graphene for metal-free catalysis, *Chem. Soc. Rev.*, 2014, **43**(8), 2841–2857, DOI: **10.1039/C3CS60401B**.

24 W. S. Hummers and R. E. Offeman, Preparation of Graphitic Oxide, *J. Am. Chem. Soc.*, 1958, **80**(6), 1339–1339, DOI: **10.1021/ja01539a017**.

25 H. J. Yu, L. Shang, T. Bian, R. Shi, G. I. N. Waterhouse, Y. F. Zhao, C. Zhou, L. Z. Wu, C. H. Tung and T. R. Zhang, Nitrogen-Doped Porous Carbon Nanosheets Templated from g-CN as Metal-Free Electrocatalysts for Efficient Oxygen Reduction Reaction, *Adv. Mater.*, 2016, **28**(25), 5080–5086, DOI: **10.1002/adma.201600398**.

26 G. Kresse and J. Furthmuller, Efficient iterative schemes for ab initio total-energy calculations using a plane-wave basis set, *Phys. Rev. B: Condens. Matter Mater. Phys.*, 1996, **54**(16), 11169–11186, DOI: **10.1103/PhysRevB.54.11169**.

27 G. Kresse and J. Furthmuller, Efficiency of ab-initio total energy calculations for metals and semiconductors using a plane-wave basis set, *Comput. Mater. Sci.*, 1996, **6**(1), 15–50, DOI: **10.1016/0927-0256(96)00008-0**.

28 G. Kresse and D. Joubert, From ultrasoft pseudopotentials to the projector augmented-wave method, *Phys. Rev. B: Condens. Matter Mater. Phys.*, 1999, **59**(3), 1758–1775, DOI: **10.1103/PhysRevB.59.1758**.

29 Y. K. Zhang and W. T. Yang, Comment on "Generalized gradient approximation made simple", *Phys. Rev. Lett.*, 1998, **80**(4), 890–890, DOI: **10.1103/PhysRevLett.80.890**.

30 S. Grimme, J. Antony, S. Ehrlich and H. Krieg, A consistent and accurate ab initio parametrization of density functional dispersion correction (DFT-D) for the 94 elements H-Pu, *J. Chem. Phys.*, 2010, **132**(15), 154104, DOI: **10.1063/1.3382344**.

31 D. Mejia-Rodriguez, A. Kunitsa, E. Aprà and N. Govind, Scalable Molecular GW Calculations: Valence and Core Spectra, *J. Chem. Theory Comput.*, 2021, **17**(12), 7504–7517, DOI: **10.1021/acs.jctc.1c00738**.

32 D. Mejia-Rodriguez, E. Aprà, J. Autschbach, N. P. Bauman, E. J. Bylaska, N. Govind, J. R. Hammond, K. Kowalski, A. Kunitsa and A. Panyala, *et al.*, NWChem: Recent and Ongoing Developments, *J. Chem. Theory Comput.*, 2023, **19**(20), 7077–7096, DOI: **10.1021/acs.jctc.3c00421**.

33 J. W. Furness, A. D. Kaplan, J. L. Ning, J. P. Perdew and J. W. Sun, Accurate and Numerically Efficient r^{2}SCAN Meta-Generalized Gradient Approximation, *J. Phys. Chem. Lett.*, 2020, **11**(21), 9248–9248, DOI: **10.1021/acs.jpclett.0c03077**.

34 S. Grimme, S. Ehrlich and L. Goerigk, Effect of the Damping Function in Dispersion Corrected Density Functional Theory, *J. Comput. Chem.*, 2011, **32**(7), 1456–1465, DOI: **10.1002/jcc.21759**.

35 J. P. Perdew, K. Burke and M. Ernzerhof, Generalized gradient approximation made simple, *Phys. Rev. Lett.*, 1996, **77**(18), 3865–3868, DOI: **10.1103/PhysRevLett.77.3865**.

36 D. Golze, L. Keller and P. Rinke, Accurate Absolute and Relative Core-Level Binding Energies from, *J. Phys. Chem. Lett.*, 2020, **11**(5), 1840, DOI: **10.1021/acs.jpclett.9b03423**.

37 L. E. Daga, B. Civalleri and L. Maschio, Gaussian Basis Sets for Crystalline Solids: All-Purpose Basis Set Libraries vs System-Specific Optimizations, *J. Chem. Theory Comput.*, 2020, **16**(4), 2192–2201, DOI: **10.1021/acs.jctc.9b01004**.

38 A. Hellweg and D. Rappoport, Development of new auxiliary basis functions of the Karlsruhe segmented contracted basis sets including diffuse basis functions (def2-SVPD, def2-TZVPPD, and def2-QVPPD) for RI-MP2 and RI-CC calculations, *Phys. Chem. Chem. Phys.*, 2015, **17**(2), 1010–1017, DOI: **10.1039/c4cp04286g**.

39 X. L. Li, H. L. Wang, J. T. Robinson, H. Sanchez, G. Diankov and H. J. Dai, Simultaneous Nitrogen Doping and Reduction of Graphene Oxide, *J. Am. Chem. Soc.*, 2009, **131**(43), 15939–15944, DOI: **10.1021/ja907098f**.

40 Y. H. Tang, X. Wang, J. J. Chen, X. X. Wang, D. J. Wang and Z. Y. Mao, Templated transformation of g-C3N4 nanosheets into nitrogen-doped hollow carbon sphere with tunable nitrogen-doping properties for application in Li-ions batteries, *Carbon*, 2020, **168**, 458–467, DOI: **10.1016/j.carbon.2020.07.022**.

41 G. Kharlamova, O. Kharlamov, M. Bondarenko and O. Khyzhun, Hetero-Carbon Nanostructures as the Effective Sensors in Security Systems, *Nanomaterials for Security*, 2016, pp. 239–258, DOI: **10.1007/978-94-017-7593-9_19**.

42 X. Y. Lu, D. Wang, L. P. Ge, L. H. Xiao, H. Y. Zhang, L. L. Liu, J. Q. Zhang, M. Z. An and P. X. Yang, Enriched graphitic N in nitrogen-doped graphene as a superior metal-free electrocatalyst for the oxygen reduction reaction, *New J. Chem.*, 2018, **42**(24), 19665–19670, DOI: **10.1039/c8nj04857f**.

43 J. J. Li, W. Y. Zan, H. X. Kang, Z. P. Dong, X. M. Zhang, Y. X. Lin, Y. W. Mu, F. W. Zhang, X. M. Zhang and J. Gu, Graphitic-N highly doped graphene-like carbon: A superior metal-free catalyst for efficient reduction of CO, *Appl. Catal., B*, 2021, **298**, 120510, DOI: **10.1016/j.apcatb.2021.120510**.

44 F. Yang, C. Chi, C. X. Wang, Y. Wang and Y. F. Li, High graphite N content in nitrogen-doped graphene as an efficient metal-free catalyst for reduction of nitroarenes in water, *Green Chem.*, 2016, **18**(15), 4254–4262, DOI: **10.1039/c6gc00222f**.

45 A. Sato, K. Gotoh, S. Sato and Y. Yamada, Toward strategical bottom-up synthesis of carbon materials with exceptionally high pyrrolic-nitrogen content: Development of screening techniques, *Carbon*, 2024, **222**, 118904, DOI: **10.1016/j.carbon.2024.118904**.

46 I. Papailias, N. Todorova, T. Giannakopoulou, N. Ioannidis, P. Dallas, D. Dimotikali and C. Trapalis, Novel torus shaped g-C3N4 photocatalysts, *Appl. Catal., B*, 2020, **268**, 118733, DOI: **10.1016/j.apcatb.2020.118733**.

47 W. Zhang, P. Oulego, T. K. Slot, G. Rothenberg and N. R. Shiju, Selective Aerobic Oxidation of Lactate to Pyruvate Catalyzed by Vanadium-Nitrogen-Doped Carbon Nanosheets, *ChemCatChem*, 2019, **11**(15), 3381–3387, DOI: **10.1002/cctc.201900819**.

48 Y. J. Qi, M. Zhang, L. Qi and Y. Qi, Mechanism for the formation and growth of carbonaceous spheres from sucrose by hydrothermal carbonization, *RSC Adv.*, 2016, **6**(25), 20814–20823, DOI: **10.1039/c5ra26725k**.

49 G. Sastre, A. Forneli, V. Almasan, V. I. Parvulescu and H. Garcia, Isotopic H/D exchange on graphenes. A combined experimental and theoretical study, *Appl. Catal., A*, 2017, **547**, 52–59, DOI: **10.1016/j.apcata.2017.08.018**.

50 K. Kuwajima, M. Yagi-Utsumi, S. Yanaka and K. Kato, DMSO-Quenched H/D-Exchange 2D NMR Spectroscopy and Its Applications in Protein Science, *Molecules*, 2022, **27**(12), 3748, DOI: **10.3390/molecules27123748**.